Precise Control of the Recollision Dynamics in Nonsequential Double Ionization by Spatially Inhomogeneous Few-Cycle Negatively Chirped Laser Pulses

Yingbin Li[†*], Fengrun Wu[†], Fanfei Liu, Shuaijie Kang, Zhengfa Li, Ke Zhang, Yifan Liu, Kuo Li, Chunyang Zhai, Jingkun Xu[*], Pu Wang, Qiming Zhao, and Benhai Yu[*]

College of Physics and Electronic Engineering, Xinyang Normal University, Xinyang 464000, China

(Received 24 January 2025; accepted manuscript online 10 April 2025)

With a three-dimensional semiclassical ensemble method, we theoretically investigated the nonsequential double ionization of Ar driven by the spatially inhomogeneous few-cycle negatively chirped laser pulses. Our results show that the recollision time window can be precisely controlled within an isolated time interval of several hundred attoseconds, which is useful for understanding the subcycle correlated electron dynamics. More interestingly, the correlated electron momentum distribution (CEMD) exhibits a strong dependence on laser intensity. That is, at lower laser intensity, CEMD is located in the first quadrant. As the laser intensity increases, CEMD shifts almost completely to the second and fourth quadrants, and then gradually to the third quadrant. The underlying physics governing the CEMD's dependence on laser intensity is explained.

DOI: 10.1088/0256-307X/42/5/053703 CSTR: 32039.14.0256-307X.42.5.053703

1. Introduction. The interaction of an intense laser pulse with atoms or molecules gives rise to various interesting nonlinear phenomena, including high-order harmonic generation (HHG),[1–4] high-order above-threshold ionization (HATI),[5–7] and nonsequential double ionization (NSDI),[8–17] among others. A series of experimental and theoretical studies have confirmed that these phenomena can be well described by the three-step recollision process,[18] in which the outermost electron undergoes tunnel ionization when the laser field reaches a sufficiently high intensity. The ionized electron is further accelerated by the oscillating laser field and returns to the parent ion when the field reverses its direction. If the ionized electron recombines with the parent ion core, high-energy photons are emitted, resulting in HHG. If the ionized electron undergoes elastic or inelastic collisions with the parent ion core, it results in HATI or NSDI respectively.

Extensive studies on NSDI have revealed numerous novel features in the correlated electron momentum distributions (CEMDs).[24–28] These features provide insights into microscopic dynamical processes, which are governed by the recollision mechanism.[19–22] For instance, a finger-like structure has been observed in the correlated longitudinal momentum distribution of helium's NSDI when driven by an 800 nm 2 PW/cm^2 laser pulse. Theoretical studies indicate that, at relatively high laser intensities, the asymmetric sharing of electron energy during the recollision process contributes to this structure.[20] In contrast, at relatively low laser intensities, both nuclear Coulomb attraction and final-state electron repulsion contribute significantly to the formation of the finger-like structure.[19] When driven by two-color laser pulses, CEMDs exhibit a narrow arc-like structure, which is attributed to the recollision time within an attosecond time interval and the recollision energy being below the second ionization potential of helium.[21] Additionally, with few-cycle laser pulses, a cross-shaped structure is observed in CEMD.[22]

Previous studies of NSDI have primarily focused on spatially homogeneous fields. In recent years, when a laser pulse is incident on a metal nanostructure, a spatially inhomogeneous field is generated in its vicinity due to plasmonic effects. Strong field ionization phenomena in the spatially inhomogeneous fields have attracted much attention.[23–30] Compared to a homogeneous field, an electron in a spatially inhomogeneous field can obtain higher energy, even reaching keV regime.[23] Such high energy leads to a significant increase in the harmonic cutoff.[31] In addition, it has been found that the photoelectron momentum distribution is strongly dependent on the carrier envelope phase (CEP) of the laser field.[24] Moreover, the spatial inhomogeneity of the laser field can substantially modify the electron trajectories and the ellipticity of emitted attosecond pulses.[29] At present, NSDI in spatially inhomogeneous laser fields remains relatively underexplored.[32,33]

Chirped laser pulses are valuable tools for probing and controlling ultrafast dynamics and have been extensively used to investigate nonlinear phenomena in strong-field ionization both experimentally and theoretically.[34–39,45] Nakajima's theoretical studies reveal that the chirp dependence in above-threshold ionization primarily originates from excited bound states, which play a more significant role than the ground state.[35] Sun *et al.* investigated photoelectron holography in strong-field ionization using few-cycle chirped laser pulses, finding that the opening and closing of the ionization channel can be precisely con-

[†]These authors contributed equally to this work.

[*]Corresponding author. Email: liyingbin2008@163.com; xujingkun@xynu.edu.cn; hnyubenhai@163.com

© 2025 Chinese Physical Society and IOP Publishing Ltd. All rights, including for text and data mining, AI training, and similar technologies, are reserved.

trolled and the holographic interference structure can be isolated by adjusting the chirp parameters.[39] For HHG, a significant extension of the cutoff can be achieved by optimizing the chirping rate parameters of a few-cycle chirped laser pulse.[34] Moreover, the CEP-dependent and chirp-dependent photoelectron spectra for few-cycle pulses have been measured. The results reveal stripe-like interference structures and demonstrate their dependence on the chirp of the laser pulse.[45]

In this work, we theoretically study the NSDI of Ar driven by spatially inhomogeneous few-cycle negatively chirped laser pulses, using the semiclassical ensemble model. Our results show that the yield curve of double ionization (DI) exhibits a pronounced "knee" structure, which is the characteristic of NSDI. By backtracking the classical trajectories, we find that the recollision time window can be precisely controlled within a 0.2-laser-cycle interval for the considered intensity range. Additionally, our results show that at low laser intensity, CEMD is primarily located in the first quadrant. As the intensity gradually increases to $0.04\,\mathrm{PW/cm^2}$, CEMD progressively shifts from the first quadrant and eventually almost entirely to the second and fourth quadrants. With further increasing in laser intensity, CEMD continues to shift from the second and fourth quadrants toward the third quadrant. The underlying physics of CEMD dependence on laser intensity is explained.

2. Methods. Due to the extensive computational demands of solving the time-dependent Schrödinger equation for a two-active-electron system in strong laser fields, the semiclassical ensemble model has been widely adopted in recent decades. Numerous studies have confirmed that this model is a reliable tool for exploring electron dynamics in strong-field ionization.[12,40–42] Moreover, the semiclassical ensemble model provides a physically intuitive picture of the recollision processes in NSDI. Therefore, we employ the three-dimensional semiclassical ensemble model to study the electron dynamics of NSDI, driven by spatially inhomogeneous, few-cycle negatively chirped laser pulses. The semiclassical model is primarily applied in the regime where the recollision impact ionization (RII) channel dominates. Besides, for the lower intensity, where the recollision-double excitation with subsequent-ionization (RDESI) channel dominates, the results from the semiclassical model are also consistent with the experimental observations.[46]

In our model, the outermost electron undergoes tunneling ionization, initially possessing zero longitudinal momentum parallel to the laser polarization direction and transverse momentum with a Gaussian-like distribution perpendicular to the laser polarization direction. The weight of each trajectory is given by the Ammosov-Delone-Krainov (ADK) theory[43,44]

$$W(t_0,\, p_\perp) \propto \Big[\frac{2(2I_{p1})^{3/2}}{|E(t_0)|}\Big]^{\frac{2}{\sqrt{2I_{p1}}}-1} \frac{\sqrt{2I_{p1}}}{|E(t_0)|} \cdot \exp\Big[-\frac{2(2I_{p1})^{3/2}}{3|E(t_0)|}\Big] \exp\Big[-p_\perp^2 \frac{\sqrt{2I_{p1}}}{|E(t_0)|}\Big]. \quad (1)$$

Here, t_0 is the tunneling time, $p_\perp$ is the initial transverse momentum, and $E(t_0)$ is the transient electric field of the laser pulse at the tunneling time. Additionally, $I_{p1} = 0.59$ a.u. is the first ionization potential of the model atom, which is equal to that of the Ar atom. The initially bound electron is determined by assuming that the electron is in the ground state of Ar^+, and its initial position and momentum distributions follow the microcanonical distribution. The subsequent evolution of the two-electron system is determined by the classical Newtonian equations,

$$\frac{\mathrm{d}^2\boldsymbol{r}_i}{\mathrm{d}t^2} = -\nabla[V_{\mathrm{ne}}(\boldsymbol{r}_i) + V_{\mathrm{ee}}(\boldsymbol{r}_1, \boldsymbol{r}_2)] - \boldsymbol{E}(t), \quad (2)$$

where $\boldsymbol{r}_i$ denotes the position of the ith electron, $V_{\mathrm{ne}}(\boldsymbol{r}_i) = -2/\sqrt{r_i^2 + a^2}$ represents the ion core-electron potential, and $V_{\mathrm{ee}}(\boldsymbol{r}_1, \boldsymbol{r}_2) = 1/\sqrt{(\boldsymbol{r}_1 - \boldsymbol{r}_2)^2 + b^2}$ is the electron–electron potential energy. To avoid self-ionization and unphysical numerical singularity, the softcore parameters a and b are set to 1.5 a.u. and 0.05 a.u., respectively. We define a double ionization event as occurring if both electrons obtain positive energies at the end of the laser pulse.

For simplicity, the spatially inhomogeneous field generated by a nanostructure is approximated as linearly decreasing. The electric field can be written as

$$\boldsymbol{E}(x,t) = E_0(1 + 2\varepsilon x)\cos[\omega t + \phi(t)]f(t)\boldsymbol{e}_x, \quad (3)$$

where E_0 is the field amplitude, $f(t) = \sin^2(\frac{\pi t}{4T})$ is the envelope pulse, T is the optical period, $\omega = 0.0456$ a.u. is the laser field frequency, and $\boldsymbol{e}_x$ is the unit vector along the x direction. Here, the inhomogeneity parameter ε is chosen to be 0.007. The phase of the chirp pulse is given by $\phi(t) = \beta[(t - t_0)/\tau_0]^2$, where β is the chirp parameter, $t_0 = 198$ a.u. adjusts the sweep range of the electric field, and $\tau_0 = 210$ a.u. controls the steepness of the chirped function. The wavelength of the pulse is set to 1000 nm. In our calculations, more than 200,000 DI trajectories are collected. Figure 1 shows the electric field for a negatively chirped laser pulse ($\beta = -3$) and a chirp-free laser pulse ($\beta = 0$). P1, P2, and P3 denote three peaks of the negatively chirped laser pulse. Compared to the chirp-free laser pulse, peak P2 is extended, while peak P3 is suppressed in the negatively chirped laser pulse. The inhomogeneous field is usually generated around nanostructure, and the degree of the inhomogeneous depends on the shape and size of the nanostructure. Note that experimentally obtaining laser pulses with the inhomogeneous and chirp parameters in our study is not simple, but they are achievable.[46–49]

The selection of inhomogeneity and chirp parameters is principally designed to manipulate the laser pulse waveform for precise regulation of the recollision time window. Specifically, an inhomogeneity parameter ε effectively diminishes the return energy of tunneling electrons at the P2 peak. The selection of the chirp parameter β requires effective suppression of P3 peak in Fig. 1.

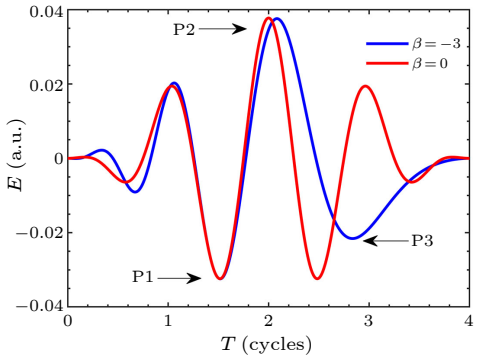

Fig. 1. The electric fields for a negatively chirped laser pulse ($\beta = -3$) and a chirp-free laser pulse ($\beta = 0$). P1, P2, and P3 denote three peaks of a negatively chirped laser pulse.

3. Results and Discussion. Figure 2 shows the yield of double ionization as a function of the laser peak intensity for the spatially inhomogeneous few-cycle negatively chirped laser pulses ($\varepsilon = 0.007$, $\beta = -3$) and the spatially inhomogeneous few-cycle laser pulse ($\varepsilon = 0.007$, $\beta = 0$). It can be seen that all the yield curves exhibit a pronounced "knee" structure, which is characteristic of the recollision process in NSDI.

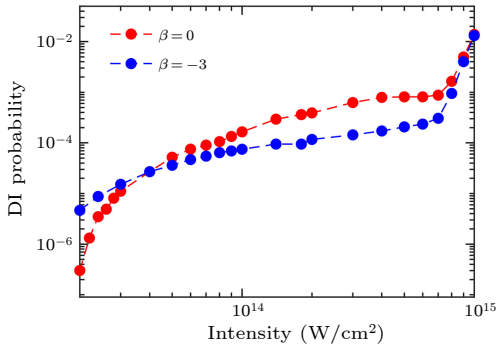

Fig. 2. The yields of double ionization (DI) as a function of the laser peak intensity for the spatially inhomogeneous few-cycle negatively chirped laser pulse (blue line, $\beta = -3$) and the spatially inhomogeneous few-cycle laser pulse (red line, $\beta = 0$).

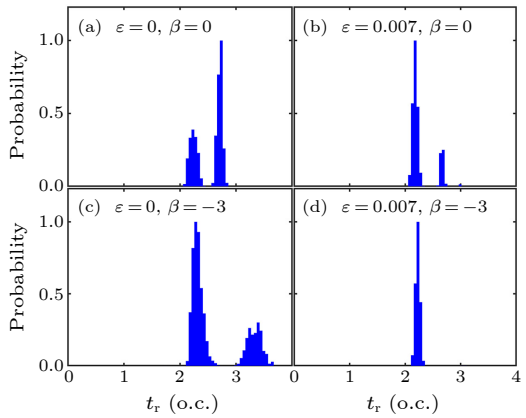

Fig. 3. The recollision time distribution for the four different laser field. (a) The few-cycle pulse ($\varepsilon = 0$, $\beta = 0$). (b) The spatially inhomogeneous pulse ($\varepsilon = 0.007$, $\beta = 0$). (c) The negatively chirped laser pulse ($\varepsilon = 0$, $\beta = -3$). (d) The spatially inhomogeneous few-cycle negatively chirped laser pulse ($\varepsilon = 0.007$, $\beta = -3$). The laser intensity is 0.09 PW/cm^2, and the laser wavelength is 1000 nm.

To demonstrate the advantages of spatially inhomogeneous few-cycle negatively chirped laser pulses in studying the recollision dynamics of NSDI, we present the recollision time distributions in Fig. 3 for four different laser fields: the few-cycle pulse ($\varepsilon = 0$, $\beta = 0$), the spatially inhomogeneous pulse ($\varepsilon = 0.007$, $\beta = 0$), the negatively chirped laser pulse ($\varepsilon = 0$, $\beta = -3$), and the spatially inhomogeneous few-cycle negatively chirped laser pulse ($\varepsilon = 0.007$, $\beta = -3$). The recollision time is defined as the instant of closest approach following the first departure of the tunneling electron from the parent ion core. It can be seen that only when driven by the spatially inhomogeneous few-cycle negatively chirped laser pulse does the recollision time distribution exhibit a single-peak structure. The difficulty in inducing NSDI for the tunneling electron ionized around peak P2, driven by the spatially inhomogeneous few-cycle negatively chirped laser pulse, arises from two inhibiting factors. First, the characteristics of the spatially inhomogeneous field result in a very low return energy for the tunneling electrons. Second, the chirped laser properties strongly suppress the P3 peak, making it challenging for the tunneling electrons to return to the parent ion core.

Figure 4(a) displays the recollision time distributions for five different laser intensities ranging from 0.01 PW/cm^2 to 0.09 PW/cm^2. Clearly, the recollision times are concentrated in a short time interval for all five laser intensities, approximately 1/5 laser cycle. Moreover, with the increase of laser intensity, the recollision time window gradually shifts to the right, which means that

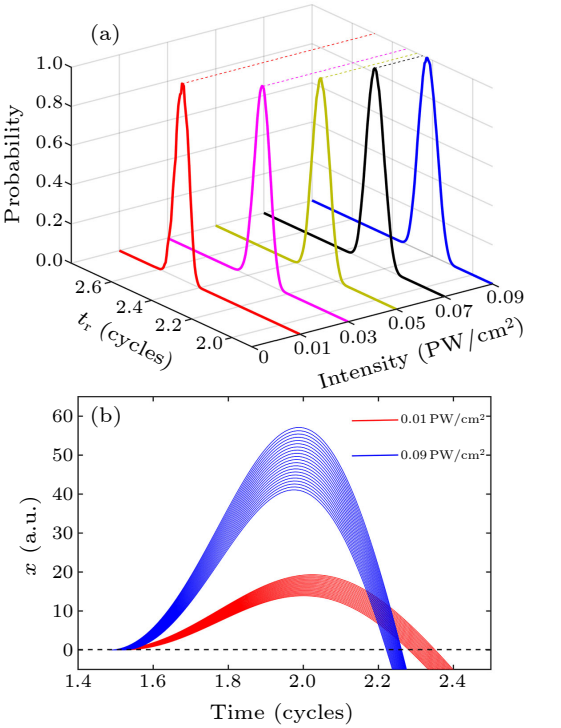

Fig. 4. (a) The distributions of recollision time for different laser intensities. The laser intensities are 0.01 PW/cm^2, 0.03 PW/cm^2, 0.05 PW/cm^2, 0.07 PW/cm^2, and 0.09 PW/cm^2, respectively. (b) Schematic diagrams of the electron classical trajectories corresponding to electron ionization along the positive x direction at 0.01 PW/cm^2 and 0.09 PW/cm^2.

the recollision occurs earlier. To understand this shift, Fig. 4(b) shows schematic diagrams of the electron classical trajectories for ionization along the positive x-axis at laser intensities of 0.01 PW/cm^2 and 0.09 PW/cm^2, using the Simple-man model. As the laser intensity increases, the electron moving along the positive x-axis travels farther from the parent ion core. When the electric field is reversed, the electrons are pulled back more quickly to the parent ion core by the stronger electric field, resulting in a shorter recollision time. Note that in the Simple-man model, the initial position and momentum of the tunneling electron are assumed to be zero, and Coulomb interaction is neglected.

By using the spatially inhomogeneous few-cycle negatively chirped laser pulse, the recollision time window can be precisely controlled within an isolated time interval of several hundred attoseconds, which is useful for understanding the subcycle correlated electron dynamics. Figures 5(a)–5(d) present CEMDs along the x-axis for the spatially inhomogeneous few-cycle negatively chirped laser pulses. The laser intensities are 0.01 PW/cm^2, 0.03 PW/cm^2, 0.05 PW/cm^2, and 0.07 PW/cm^2, respectively. At an intensity of 0.01 PW/cm^2, CEMD is located in the first quadrant and exhibits a V-shaped structure, as shown in Fig. 5(a). When the laser intensity is increased to 0.03 PW/cm^2, CEMD becomes almost concentrated in the second and fourth quadrants [see Fig. 5(b)], indicating that the correlated electron pair is emitted into the opposite direction. As the laser intensity further increases to 0.05 PW/cm^2 and 0.07 PW/cm^2, CEMDs exhibit an arc-like structure, and the highest concentration gradually shifts towards the third quadrant [see Figs. 5(c) and 5(d)]. Figure 5(e) shows the proportions of CEMD in the first quadrant (blue circles), the second and fourth quadrants (green diamonds), and the third quadrant (red squares) as the laser intensity changes. The results show that the dependence of CEMD on the laser intensity involves two distinct processes: Process A, at low laser intensity, CEMD is primarily located in the first quadrant. As the intensity gradually increases to 0.04 PW/cm^2, CEMD progressively moves from the first quadrant and eventually shifts almost entirely to the second and fourth quadrants; Process B, with further increases in intensity, CEMD continues to shift from the second and fourth quadrants towards the third quadrant. In the following, we will demonstrate how laser intensity influences CEMD in these two processes. We categorize CEMD shift into two processes: Process A (low intensity, RDESI-dominated) and Process B (high intensity, RII-dominated).

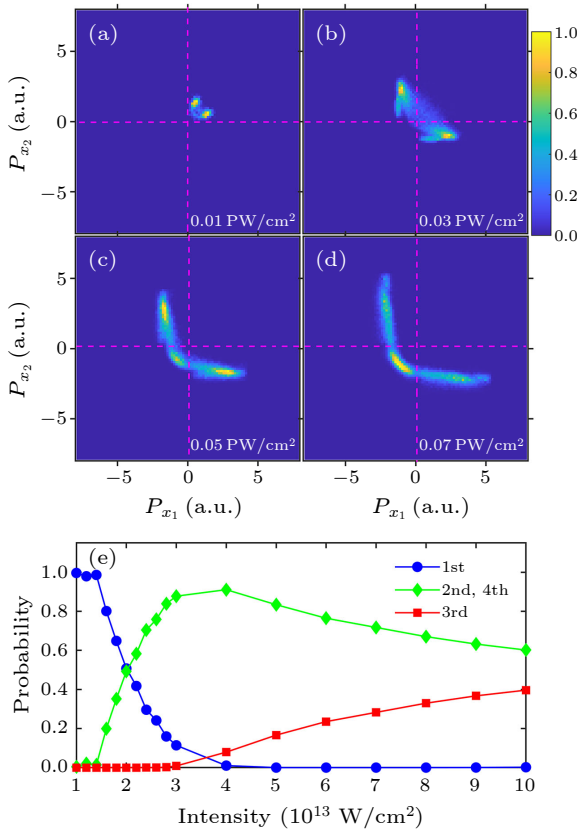

Fig. 5. (a)–(d) CEMDs in the direction parallel to the laser field. The laser intensities are 0.01 PW/cm^2, 0.03 PW/cm^2, 0.05 PW/cm^2, and 0.07 PW/cm^2, respectively. (e) The proportions of CEMD in the first quadrant, second and fourth quadrants, and third quadrant for different laser intensities.

For Process A, when the laser intensity is 0.01 PW/cm^2, the return energy of the tunneling electron is low. In this case, NSDI mechanism follows RDESI channel. As the laser intensity increases, the return energy of the tunneling electron also increases, which causes a transition in NSDI mechanism to the recollision-single excitation with subsequent-ionization (RSESI) channel. Figure 6 shows two typical NSDI trajectories corresponding to RDESI channel (the left column) and RSESI channel (the right column). We examine the time evolutions of the longitudinal momenta, the x-coordinate in the polarization direction, and energies of the two electrons.

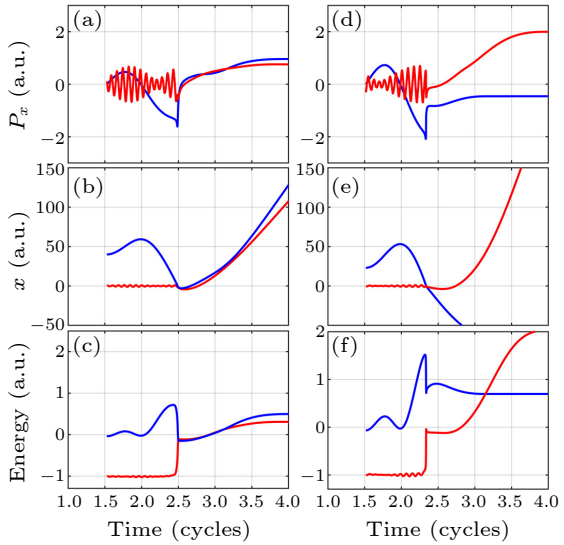

Fig. 6. Two typical NSDI trajectories for RDESI channel (the left column) and RSESI channel (the right column). The panels from top to bottom show the longitudinal momenta, coordinate x in polarization direction, and energies of two electrons versus the time, respectively.

For RDESI channel, both electrons enter an excited state after the recollision and are subsequently pulled out by the laser electric field, emitted in the positive direction [see Fig. 6(b)]. In RSESI channel, the tunneling electron retains a significant amount of energy after recollision, allowing it to rapidly move away from the parent ion along the negative x-axis and be emitted in the negative direction [see Fig. 6(e)]. Thus, as the laser intensity increases, the transition from RDESI channel to RSESI channel causes CEMD to gradually shift from the first quadrant to the second and fourth quadrants [see Fig. 5(e)]. For RDESI, it primarily involves backward scattering due to the low return energy. On the other hand, for RSESI, the return energy is higher, and the electron quickly passes though the vicinity of the parent ion core, resulting in forward scattering.

For Process B, the return energy of the tunneling electron exceeds the second ionization potential. Consequently, the dominant mechanism of NSDI is RII channel. Figure 7(a) shows the statistical distribution of the energy difference (ΔE) between the correlated electron pair at the instant of 0.03 T after recollision for 0.05 PW/cm^2. The value of ΔE indicates the degree of asymmetric energy sharing during recollision. A larger ΔE indicates more asymmetric energy sharing between the two electrons, and *vice versa*. One can see that ΔE extends up to a maximum value of about 3 a.u.. Here, we divide the ΔE distribution into two regions: region I ($\Delta E < 0.6$ a.u.) and region II ($\Delta E > 0.6$ a.u.). CEMDs for these two regions are shown in Figs. 7(d) and 7(e), respectively. CEMD for all NSDI events is shown in Fig. 7(c) for comparison. CEMD for region I is mostly located in the third quadrant.

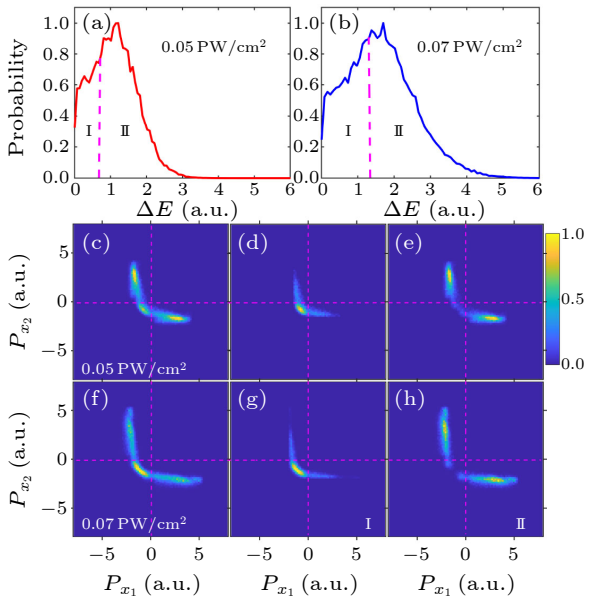

Fig. 7. (a) and (b) The distributions of kinetic energy difference at the instant of 0.03 T after recollision at 0.05 PW/cm^2 and 0.07 PW/cm^2, respectively. The distributions are divided into two regions I and II, quantifying the degree of energy sharing asymmetry. (c) CEMDs at 0.05 PW/cm^2. (d) and (e) CEMDs corresponding to the two regions in (a). (f) CEMDs at 0.07 PW/cm^2. (g) and (h) CEMDs corresponding to the two regions in (b).

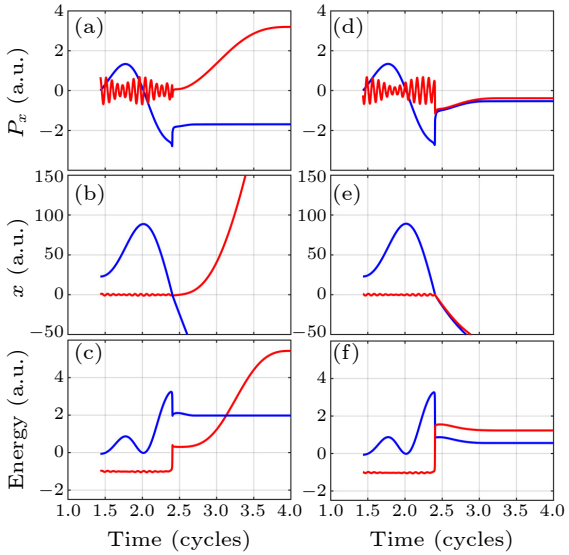

Fig. 8. Two typical NSDI trajectories. The panels from top to bottom show the longitudinal momenta, coordinate x in polarization direction, and energies of two electrons versus the time, respectively. For NSDI trajectory in the left column, two electrons experience asymmetric energy sharing during the recollision. For NSDI trajectory in the right column, two electrons experience symmetric energy sharing during the recollision.

For region II, the majority of CEMD is concentrated in the second and fourth quadrants. The results for 0.07 PW/cm^2 are also shown in Figs. 7(b) and 7(f)–7(h). One can see that the distributions of the energy difference ΔE extends up to approximately 5 a.u. This indicates that asymmetric energy sharing becomes more pronounced as the laser intensity increases. Similarly, varying degrees of asymmetric energy sharing can also cause the correlated electron pair to be emitted in opposite or the same directions. However, at higher laser intensity, region I and region II are separated by the greater degree of asymmetric energy sharing, i.e., $\Delta E = 1.2$ a.u.

To intuitively understand the dependence of CEMD on asymmetric and symmetric energy sharing, Fig. 8 shows two typical NSDI trajectories: one for asymmetric energy sharing (left column) and the other for symmetric energy sharing (right column). For asymmetric energy sharing, the tunneling electron transfers less energy to the second electron and quickly moves away from the parent ion along the negative x-axis. Thus, the second electron, gaining limited energy during recollision, is emitted with near-zero velocity. After recollision, the electric field reverses at 2.47 T, and the second electron is eventually emitted along the positive x-axis [see Figs. 8(a) and 8(b)]. This results in CEMD being located in the second and fourth quadrants. In contrast, with symmetric energy sharing, both electrons move away from the parent ion along the negative x-axis at similar speeds after recollision [see Figs. 8(d) and 8(e)], leading to CEMD being located in the third quadrant.

Interestingly, regions I and II are separated by different ΔE values in Figs. 7(a) and 7(b). This suggests that at higher laser intensities, stronger symmetric energy sharing during recollision allows the correlated electron pair to be emitted in the opposite direction. As a result,

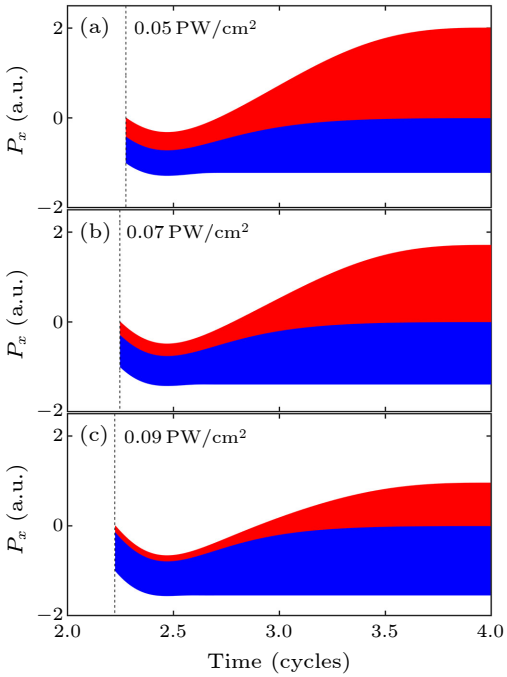

Fig. 9. The classical momentum evolution of the electron with initial momentum ranging from −1 a.u. to 0 a.u. for the laser intensities of 0.05 PW/cm^2 (a), 0.07 PW/cm^2 (b), and 0.09 PW/cm^2 (c), respectively. The ionization time corresponds to the peak value of the recollision time distribution shown in Fig. 4(a). The red lines represent trajectories with final momentum greater than zero, while the blue lines represent trajectories with final momentum less than zero.

the proportion of CEMD in the second and fourth quadrants decreases with increasing laser intensity [see Fig. 5(e)]. To explain this, we use the Simple-man model to show the time evolution of the electrons' momentum for initial momenta ranging from −1 a.u. to 0 a.u., at laser intensities of 0.05 PW/cm^2, 0.07 PW/cm^2, and 0.09 PW/cm^2 in Fig. 9. Electrons are released at the peak of the recollision time distribution, with corresponding recollision times of 2.276 T, 2.249 T, and 2.226 T for the three laser intensities. At a laser intensity of 0.05 PW/cm^2, electrons with initial momenta between −0.4 a.u. and 0 a.u. exhibit positive final momenta (red lines), while those with initial momenta between −1 a.u. and −0.4 a.u. exhibit negative final momenta (blue lines). As the laser intensity increases to 0.07 PW/cm^2 and 0.09 PW/cm^2, the shift in recollision time results in a gradual reduction of the red region. Specifically, for these two laser intensities, the electrons with initial momenta ranging from −0.28 a.u. to 0 a.u. and from −0.13 a.u. to 0 a.u. exhibit positive final momenta. As laser intensity increases, the more demanding degree of symmetric energy sharing between the electron pair during recollision causes CEMD to gradually shift from the second and fourth quadrants to the third quadrant [see Fig. 5(e)].

4. Conclusion. In conclusion, using the semiclassical 3D ensemble model, we have investigated the recollision dynamics of NSDI in spatially inhomogeneous few-cycle negatively chirped laser pulses. The yield curve for double ionization exhibits a pronounced "knee" structure, which is the characteristic of NSDI. Our back analysis shows that the recollision time window can be precisely controlled within an isolated time interval of several hundred attoseconds, which is previously challenging to achieve. This isolated narrow recollision time window helps understanding the subcycle correlated electron dynamics in NSDI, and can also be applied to other strong-field physics studies.

Due to the isolated narrow recollision time window, a clear transformation of CEMD can be observed as the laser intensity increases. At lower laser intensities, RDESI channel dominates, and CEMD is primarily located in the first quadrant. As the intensity increases, a transition to RSESI channel occurs, causing CEMD to shift towards the second and fourth quadrants. When the laser intensity increases to 0.04 PW/cm^2, RII channel dominates, and the asymmetric energy sharing results in the correlated electron pair emitting into the opposite direction. With further increase in laser intensity, the recollision time advances. The more demanding degree of symmetric energy sharing causes CEMD to gradually shift from the second and fourth quadrants to the third quadrant. Thus, the spatially inhomogeneous few-cycle negatively chirped laser pulse offers a novel way to control the electron correlation in NSDI precisely.

Acknowledgments. This work was supported by the National Natural Science Foundation of China (Grant No. 12074329) and Nanhu Scholars Program for Young Scholars of Xinyang Normal University.

References

[1] Zhao B J, Zhao J L, and Gan X T 2024 *Chin. Phys. Lett.* **41** 104201
[2] Qiao Y, Chen J Q, Zhou S S, Chen J G, Jiang S C, and Yang Y J 2024 *Chin. Phys. Lett.* **41** 014205
[3] Zhai C Y, Wu Y M, Liu Y F, Zhang K, Kang S J, Li Z F, Wu F R, Dong X Z, Cheng X Y, Li Y B, Tang Q B, and Yu B H 2024 *Results Phys.* **58** 107518
[4] Zhai C Y, Liu Y F, Li X, Liu X, Wu F R, Kang S J, Li Z F, Dong X Z, Li Y B, Tang Q B, Zhu X S, and Yu B H 2024 *Phys. Rev. A* **110** 033507
[5] Agostini P, Fabre F, Mainfray G, Petite G, and Rahman N K 1979 *Phys. Rev. Lett.* **42** 1127
[6] Paulus G G, Nicklich W, Xu H L, Lambropoulos P, and Walther H 1994 *Phys. Rev. Lett.* **72** 2851
[7] Becker W, Grasbon F, Kopold R, Milošević D B, Paulus G G, and Walther H 2002 *Adv. Atom. Mol. Opt. Phys.* **48** 35
[8] He T T, Liu Z C, Liao J Y, Li Y B, Yu B H, and Huang C 2024 *Phys. Rev. A* **109** 043109
[9] Chen J, Liu J, Fu L B, and Zheng W M 2000 *Phys. Rev. A* **63** 011404
[10] Li Y B, Wang X, and Yu B H 2016 *Sci. Rep.* **6** 37413
[11] Li Y B, Yu B H, Tang Q B, Wang X, Hua D Y, Tong A H, Jiang C H, Ge G X, Li Y C, and Wan J G 2016 *Opt. Express* **24** 6469
[12] Wang Y L, Xu S P, Wei Q, Gong C, Lai X Y, Hu S L, Liu M Q, Chen J, and Liu X J 2016 *Phys. Rev. A* **94** 053412
[13] Xu J K, Li Y B, Tian Y D, Kang S J, Liu F F, Wang Y C, Zhai C Y, Yu B H, Lu P X, and Zhou Y M 2024 *Opt. Express* **32** 33452
[14] Chen Z H, Su J, Zeng X, Huang X F, Li Y B, and Huang C 2021 *Opt. Express* **29** 29576

[15] Li Y B, Qin L L, Liu A H, Zhang K, Tang Q B, Zhai C Y, Xu J K, Chen S, Yu B H, and Chen J 2022 *Chin. Phys. Lett.* **39** 093201
[16] Li H Y, Chen J, Jiang H B, Liu J, Fu P M, Gong Q H, Yan Z C, and Wang B B 2009 *Chin. Phys. Lett.* **26** 104207
[17] Zhou Y M, Liao Q, Huang C, Tong A H, and Lu P X 2010 *Chin. Phys. Lett.* **27** 123201
[18] Corkum P B 1993 *Phys. Rev. Lett.* **71** 1994
[19] Ye D F, Liu X, and Liu J 2008 *Phys. Rev. Lett.* **101** 233003
[20] Zhou Y M, Liao Q, and Lu P X 2010 *Phys. Rev. A* **82** 053402
[21] Zhou Y M, Liao Q, Zhang Q B, Hong W Y, and Lu P X 2010 *Opt. Express* **18** 632
[22] Huang C, Zhou Y M, Zhang Q B, and Lu P X 2013 *Opt. Express* **21** 11382
[23] Ciappina M F, Perez-Hernandez J A, Shaaran T, Biegert J, Quidant R, and Lewenstein M 2012 *Phys. Rev. A* **86** 023413
[24] Ciappina M F, Perez-Hernandez J A, Shaaran T, Roso L, and Lewenstein M 2013 *Phys. Rev. A* **87** 063833
[25] Wang Z, Lan P F, Luo J H, He L X, Zhang Q B, and Lu P X 2013 *Phys. Rev. A* **88** 063838
[26] Du T Y, Guan Z, Zhou X X, and Bian X B 2016 *Phys. Rev. A* **94** 023419
[27] Wachtler F and Santos L 2016 *Phys. Rev. A* **93** 061603
[28] Ortmann L and Landsman A S 2018 *Phys. Rev. A* **97** 023420
[29] Schoeberl M R and Smith A K 1986 *J. Atmos. Sci.* **43** 1074
[30] Sun Y, Wang Z, Huo X X, and Liu X S 2022 *Phys. Rev. A* **105** 043115
[31] Husakou A, Im S J, and Herrmann J 2011 *Phys. Rev. A* **83** 043839
[32] Osika E N, Chacon A, Ortmann L, Suarez N, PerezHernandez J A, Szafran B, Ciappina M F, Sols F, Landsman A S, and Lewenstein M 2017 *Phys. Rev. X* **7** 021017
[33] Xu J K, Li Y B, Zhou Y M, Chen Y K, Li M, Yu B H, and Lu P X 2022 *Opt. Express* **30** 15951
[34] Carrera J J and Chu S 2007 *Phys. Rev. A* **75** 033807
[35] Nakajima and Takashi 2007 *Phys. Rev. A* **75** 053409
[36] Li P C, Zhou X X, Wang G L, and Zhao Z X 2009 *Phys. Rev. A* **80** 053825
[37] Peng L Y, Tan F, Gong Q H, Pronin E A, and Starace A F 2009 *Phys. Rev. A* **80** 013407
[38] Wu J, Zhang G T, Xia C L, and Liu X S 2010 *Phys. Rev. A* **82** 013411
[39] Sun Y, Wang Z, Li C W, and Liu X S 2022 *Phys. Rev. A* **106** 033116
[40] Fu L B, Liu J, Chen J, and Chen S G 2001 *Phys. Rev. A* **63** 043416
[41] Fu L B, Liu J, and Chen S G 2002 *Phys. Rev. A* **65** 021406
[42] Hao X L, Li W D, Liu J, and Chen J 2011 *Phys. Rev. A* **83** 053422
[43] Delone N B and Krainov V P 1991 *J. Opt. Soc. Am. B* **8** 1207
[44] Zhao L, Dong J W, Lv H, Yang T X, Lian Y, Jin M X, Xu H F, Ding D J, Hu S L, and Chen J 2016 *Phys. Rev. A* **94** 053403
[45] Zille D, Adolph D, Möller M, Sayler A M, and Paulus G G 2018 *New J. Phys.* **20** 063018
[46] Lin K, Chen X, Eckart S, Jiang H, Hartung A, Trabert D, Fehre K, Rist J, Schmidt L P, Schoffler M S, Jahnke T, Kunitski M, He F, and Dorner R 2022 *Phys. Rev. Lett.* **128** 113201
[47] Herink G, Solli D, Gulde M, and Ropers C 2012 *Nature* **483** 190
[48] Kim S, Jin J, Kim Y, Park I, Kim Y, and Kim S 2008 *Nature* **453** 757
[49] Kim H, Garg M, Mandal S, Seiffert L, Fennel T, and Goulielmakis E 2023 *Nature* **613** 662